RSC Advances

PAPER

View Article Online
View Journal | View Issue



Cite this: *RSC Adv.*, 2017, **7**, 38119

# Fabrication of flower-like $MoS_2/TiO_2$ hybrid as an anode material for lithium ion batteries†

Xiaoquan Zhu,[a] Xiaoyu Liang,[b] Xiaobin Fan *[a] and Xintai Su *[b]

A three-dimensional (3D) flower-like $MoS_2/TiO_2$ nanohybrid was synthesized *via* a two-step hydrothermal method. It is found that the $MoS_2/TiO_2$ nanohybrid is assembled with $MoS_2$ nanosheets and $TiO_2$ nanoparticles. The $TiO_2$ nanoparticles are homogeneously dispersed on the $MoS_2$ nanosheets. Moreover, the $MoS_2/TiO_2$ nanohybrid displays excellent electrochemical performance with a high reversible capacity of 801 mA h $g^{-1}$ at a current density of 100 mA $g^{-1}$ after 50 cycles. It also demonstrates outstanding rate behavior with a reversible discharge capacity of 660 mA h $g^{-1}$ at a current density of 1000 mA $g^{-1}$ and retains a capacity of about 760 mA h $g^{-1}$ as the current density is returned back to 100 mA $g^{-1}$. Compared with $MoS_2$, the $MoS_2/TiO_2$ nanohybrid displays enhanced cycling stability and superior rate capability. The excellent electrochemical performance may be attributed to the favorable synergistic effect between $MoS_2$ and $TiO_2$. The $TiO_2$ particles may enhance the structure stability and shorten the transport distance of ions across the surface.

Received 6th June 2017
Accepted 27th July 2017

DOI: 10.1039/c7ra06294j

rsc.li/rsc-advances



## 1. Introduction

Lithium-ion batteries (LIBs) are now one of the most important power sources for many electronic devices in our daily life. Development of rechargeable LIBs with longer cycle life and higher power density is of great interest to accommodate the growing demands for higher energy density electronic devices.[1] Currently, graphite has been widely used as the negative electrode in commercial LIBs due to its natural abundance and stable cycling performance. However, it has a relatively low theoretical capacity (372 mA h $g^{-1}$).[2] Therefore, alternative anode materials with higher specific capacity and good cycling behavior are desirable for LIBs.

In recent years, two-dimensional layered transition-metal dichalcogenides (TMDs) have attracted great interest in the field of electrochemical energy storage and conversion because of their unique physical and chemical properties. Due to their short path length and more channels for lithium ion diffusion and insertion, these 2D materials exhibit enhanced electrochemical performances as electrode materials for LIBs, such as $WS_2$, $MoS_2$.[3–5] In particular, molybdenum disulfide ($MoS_2$) has gradually drawn attention as a potential candidate, owing to its high theoretical specific capacity (~670 mA h $g^{-1}$).[6] Meanwhile, the weak van der Waals forces allow a fast diffusion path for lithium-ion and easy lithium ion insertion/extraction.[7] This is due to the layered structure of $MoS_2$. $MoS_2$ is consisting of molybdenum atoms sandwiched between two layers of closely packed sulfur atoms, two molecular layers are weakly linked by van der Waals interactions.[8] Various $MoS_2$ nanostructures such as nanoplates,[6] nanowall,[9] nanotube[10] and nanoflowers[11,12] have been reported for lithium storage as LIBs anodes. However, the inferior cycling stability due to large volume changes significantly limits its practical applications. To overcome the defects of the $MoS_2$-based electrode materials, one doable strategy is to design hybridization. A strategy is to immobilize $MoS_2$ nanostructures on carbon-based substrate to construct nanocomposites.[13–16] Most of the previous studies focused on $MoS_2$–carbon nanocomposites. Carbon tubes, carbon nanofibers, graphene and organic conducting polymers are used as carbonaceous materials.[1,10,17] However, the excessive interface between porous carbonaceous materials and electrolytes cause considerable side reactions, forming a thick solid electrolyte interface (SEI) on the carbon and leading to a low initial coulombic efficiency of <70%.[13]

Recently, some transition metal oxides were used to improve the cycling performance of $MoS_2$, such as $Fe_3O_4$ and $TiO_2$.[18,19] Titanium dioxide ($TiO_2$) has been widely used as anode material for LIBs. It possesses a low volume variation (<4%) and displays good cycling stability during the charge–discharge process.[20] Furthermore, it is a safer material compared to graphite because of its higher operation voltage (1.7 V *vs.* $Li^+/Li$). Accordingly, by combining the individual constituents, the hybrid $MoS_2/TiO_2$ system shows some merits that not exist in a single system. The advantages of both high reversible capacity and superior cycling stability are expected. The strain of volume

[a]State Key Laboratory of Chemical Engineering, School of Chemical Engineering and Technology, Collaborative Innovation Center of Chemical Science and Engineering, Tianjin University, No. 135, Yaguan Road, Jinnan District, Tianjin 300354, China. E-mail: xiaobinfan@tju.edu.cn

[b]Department of Chemistry, Zhejiang Sci-Tech University, Xiasha Campus, Hangzhou 310018, China. E-mail: suxintai827@163.com

† Electronic supplementary information (ESI) available. See DOI: 10.1039/c7ra06294j

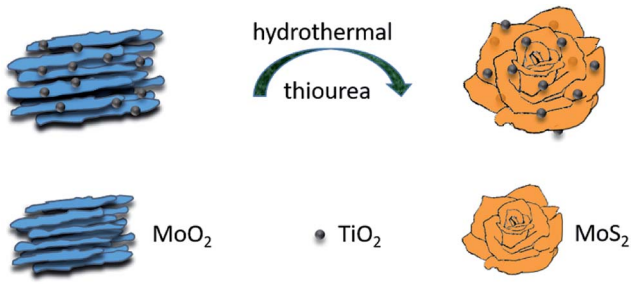


Fig. 1 Schematic illustration of the formation process of $MoS_2/TiO_2$ nanohybrid.

variation of $MoS_2$ can be alleviated. To the best of our knowledge, a number of $MoS_2/TiO_2$ hybrid systems have been widely investigated as photocatalysts.[21] However, this hybrid system has also been studied as electrode materials for LIBs in recent years.[19,22] There has some literatures reported about the applications of $TiO_2$@$MoS_2$ composite in lithium ion batteries. Li *et al.* synthesized the hierarchical $TiO_2$ nanowire@$MoS_2$ nanosheet nanocomposite by a glucose-assisted hydrothermal approach, and it displays a specific capacity of around 600 mA h $g^{-1}$ at a current density of 100 mA $g^{-1}$ after 100 cycles.[7] Xu *et al.* synthesized $MoS_2$ nanosheet@$TiO_2$ nanotube hybrid by a two-step method, and it exhibits a capacity of 472 mA h $g^{-1}$ at a current density of 100 mA $g^{-1}$ after 100 cycles.[20] The $TiO_2$ decorated few-layers $MoS_2$ nanosheets through one-pot method have been reported by our team.[23] However, we found that the $MoS_2/TiO_2$ nanohybrid derived from the $MoO_2/TiO_2$ precursor was very different from one-pot method. We consider that the morphology of the $MoO_2$ precursor plays an important role in the formation of product. Meanwhile, $TiO_2$-decorated three dimensional (3D) $MoS_2$ nanoflowers have rarely been studied as electrode materials for LIBs.

Herein, we report a two-step hydrothermal route to prepare 3D Hierarchical $MoS_2/TiO_2$ nanoflowers. The synthetic process is illustrated in Fig. 1. Firstly, the hydrothermal method was adopted to prepare the $MoO_2/TiO_2$ precursor. Secondly, the as-prepared the $MoO_2/TiO_2$ nanobundles were vulcanized by thiourea under a subsequent hydrothermal process. We supposed that the formation of 3D flower-like architecture may undergo a self-assembling process from the precursor. The as-prepared flower-like $MoS_2/TiO_2$ nanohybrid was further treated at 500 °C in an Ar atmosphere to increase its crystallinity. Finally, the $MoS_2/TiO_2$ nanohybrid exhibited enhanced electrochemical performances as an anode material. It delivered a high reversible capacity of 801 mA h $g^{-1}$ at a current density of 100 mA $g^{-1}$ after 50 cycles, and an outstanding rate behavior of a reversible discharge capacity of 660 mA h $g^{-1}$ at a current density of 1000 mA $g^{-1}$ and retains a capacity of about 760 mA h $g^{-1}$ as the current density is back to 100 mA $g^{-1}$.

## 2. Experimental section

### 2.1 Synthesis and characterization of samples

All reagents were analytical grades. The synthesis process of $MoS_2/TiO_2$ nanoflowers involves two steps: formation of the precursor $MoO_2/TiO_2$ and sequent vulcanization to $MoS_2/TiO_2$ by hydrothermal method.

**The synthesis of $MoO_2/TiO_2$ precursor.** The 2.89 mmol of $(NH_4)_6Mo_7O_{24}$ was dissolved in 30 mL of distilled water. The 2.82 g of ethanol solution of titanium tetrachloride (34% w/w) was added to the above aqueous solution under stirring. Then the mixture was stirred for 2 h. The obtained solution was transferred into a 100 mL autoclave Teflon vessel, which was filled with distilled water up to 60% of the total volume, sealed and hydrothermally treated at 180 °C for 48 h. After cooling to room temperature. The obtained precursor was collected by centrifugation and washed with distilled water and absolute ethanol several times, and dried at 60 °C for 12 h in an oven.

**The synthesis of flower-like $MoS_2/TiO_2$ nanohybrid.** 0.1423 g of $MoO_2/TiO_2$ precursor and an appropriate amount of thiourea were dissolved in 30 mL of distilled water, the mixture was stirred for 2 h, then transferred into a 100 mL Teflon-lined stainless steel autoclave, which was filled with distilled water up to 60% of the total volume. The autoclave was heated at 200 °C for 48 h. After cooling to room temperature. The product was washed more than three times with distilled water and absolute alcohol and then dried at 60 °C in the vacuum oven for 12 h. In order to improve the crystallinity, the product was calcined at 500 °C in Ar atmosphere for 4 h.

**The synthesis of bare $MoS_2$.** 0.137 mmol of $(NH_4)_6Mo_7O_{24}$ and 6.72 mmol of thiourea were dissolved in 30 mL of distilled water, then the mixture was stirred for 2 h. The obtained solution was transferred into a 100 mL Teflon-lined stainless steel autoclave, which was filled with distilled water up to 60% of the total volume. The subsequent procedure was the same as $MoS_2/TiO_2$ nanohybrid.

The composition and phase of the precursor and the final product were characterized by a Rigaku D/max-ga X-ray diffractometer (XRD) at a scanning rate of 6° $min^{-1}$ in $2\theta$ ranging from 10° to 80° with Cu K$\alpha$ radiation ($\lambda$ = 1.54178 Å). The transmission electron microscopy (TEM) were carried out on a Hitachi H-600 transmission electron microscope with accelerating voltage of 100 kV, and field-emission scanning electron microscope (FESEM, Hitachi S-4800) were obtained with an acceleration voltage of 5 kV. Thermogravimetric analysis (TGA) was carried out using a SDTQ600 at a heating rate of 10 °C $min^{-1}$ from 25 °C to 650 °C under air atmosphere. The X-ray photoelectron spectroscopy (XPS) was analyzed by Perkin-Elmer PHI1600 spectrometer.

### 2.2 Electrochemical measurement

The electrochemical tests were carried out in coin cells. The working electrodes were fabricated by coating a slurry containing 80 wt% of active materials ($MoS_2/TiO_2$ nanohybrid, $MoS_2$), 10 wt% of acetylene black, and 10 wt% of polyvinylidene fluoride (PVDF) dissolved in *N*-methyl-2-pyrrolidinone onto a copper foil and dried at 110 °C in vacuum for 12 h before pressing. The standard CR-2032 type coin cells were assembled in an Ar-filled glove box using the as-prepared anode, lithium foil as counter electrode, and Celgard-2400 as a separator. The electrolyte was 1 M $LiPF_6$ dissolved in a mixture of ethylene

 

carbonate and diethyl carbonate (EC–DEC, 1 : 1 in volume). The cells were aged for 12 h before the measurements. Cyclic voltammetry measurements (CV) and electrochemical impedance spectroscopy (EIS) were performed on an electrochemical workstation (CHI 660D). The voltage scan rate for the CV measurement was at a scan rate of 0.1 mV $s^{-1}$ over the potential range of 0.01–3.0 V (*vs.* $Li^+/Li$). The EIS data were obtained by applying excitation amplitude of 10 mV in the frequency range from 10 mHz to 1 MHz. The galvanostatic charge–discharge tests were conducted on the battery measurement system (LAND CT2001A, China) at current densities of 50–1000 mA $g^{-1}$ with a cut off voltage range of 0.01–3.0 V *vs.* $Li/Li^+$ at room temperature.

## 3. Results and discussions

### 3.1 Structural characteristics of samples

Fig. 2a shows that all the diffraction peaks of precursor can be assigned to the anatase $TiO_2$ (JCPDS 21-1272) and monoclinic $MoO_2$ phase (JCPDS 32-0671). Peaks in Fig. 2b can be indexed to a mixture of the hexagonal $MoS_2$ phase (JCPDS 74-0932) and a phase of anatase $TiO_2$ (JCPDS 21-1272). It indicated that the $MoO_2$ has been successfully transformed to $MoS_2$. The (002) diffraction peak at 13.8° is lower than standard card ($2\theta = 14°$), which indicates enlarged layer distances of $MoS_2$.

Fig. 3a and b show low and high magnification FESEM images of the annealed $MoS_2/TiO_2$ nanohybrid, respectively. It exhibits 3D flower-like structure assembled from several thin nanosheets. Some $TiO_2$ nanoparticles were decorated on the $MoS_2$ nanosheets. The TEM images of annealed $MoS_2/TiO_2$ are shown in Fig. 3c and d. And we found that the hierarchical $MoS_2/TiO_2$ nanohybrid was assembled from curly $MoS_2$ nanosheets and an amount of $TiO_2$. The $TiO_2$ nanoparticles with diameter of ~20 nm are uniformly distributed on the $MoS_2$ nanosheets. The morphology of bare $MoS_2$ were shown in Fig. S1.† It exhibits the cluster-like morphology. The TEM images of precursor $MoO_2/TiO_2$ are shown in Fig. S2.† It exhibits a small amount of $TiO_2$ nanoparticles are attached to the surface of $MoO_2$ bundles. The HRTEM image of the $MoS_2/TiO_2$ nanohybrid illustrates the crystal lattice structure of $MoS_2$ and $TiO_2$ (Fig. S3†). The interplanar spacing of 0.64 nm and 0.35 nm are corresponding to the lattice plane (002) of $MoS_2$ and (101) of $TiO_2$, respectively. The spacing is slightly larger than the layer-to-layer spacing of 6.2 Å in bulk $MoS_2$. This is consistent with the results of XRD. It also indicates that the $MoO_2$ nanobundles turn into $MoS_2$ nanosheets successfully. Moreover, the XPS of bare $MoS_2$ and $MoS_2/TiO_2$ nanohybrid were shown in the ESI (Fig. S4†). The binding energies of S $2p_{1/2}$, S $2p_{3/2}$, Mo $3d_{3/2}$ and Mo $3d_{5/2}$ peaks in the bare $MoS_2$ locate at 163.4, 162.3, 232.7 and 229.5 eV, respectively. However, the S $2p_{1/2}$, S $2p_{3/2}$, Mo $3d_{3/2}$ and Mo $3d_{5/2}$ peaks of $MoS_2/TiO_2$ nanohybrid shift to 163.2, 162.1, 232.4 and 229.2 eV, respectively. The binding energy shifts to lower binding energy mean electronic interaction between $MoS_2$ and $TiO_2$.[24]

TGA was carried out from 25 °C to 700 °C in air flow to determine the amount of $MoS_2$ in the $MoS_2/TiO_2$ nanohybrid (Fig. 4). The weight loss stage below 300 °C is a result of the evaporation of physically adsorbed water and the loss of chemisorbed water, and a large continuous weight loss in the range of approximately 300–500 °C which was caused by the oxidation of $MoS_2$. The second weight loss was measured to be 10.56% and 12.32% for the $MoS_2/TiO_2$ nanohybrid and bare $MoS_2$ nanoclusters, respectively. The result is attributed to the oxidation of $MoS_2$ to $MoO_3$. The mass fraction of $MoS_2$ in the $MoS_2/TiO_2$ nanohybrid can thus be estimated to be about 85.7 wt%. Let the weight percentage of $MoS_2$ in the $MoS_2/TiO_2$ nanohybrid to be $x$, one has $10.56 = 12.32x$. Therefore $x = 85.71\%$.[25]

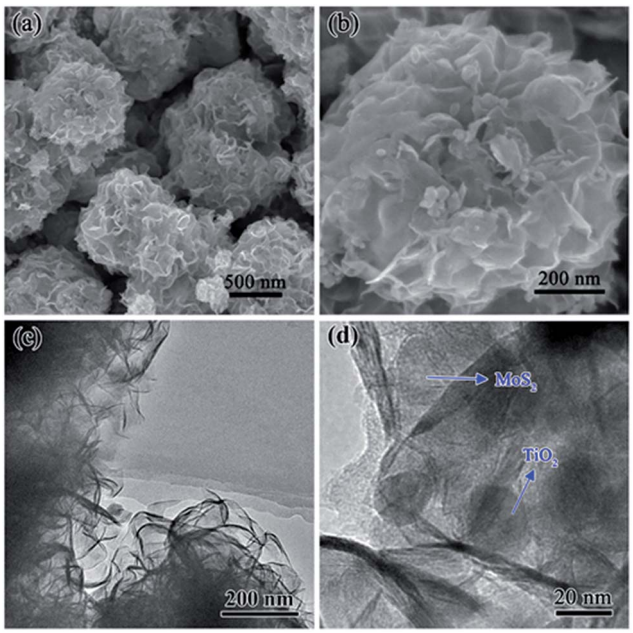


Fig. 3 (a) Low- and (b) high-magnification FESEM images of 3D $MoS_2/TiO_2$ nanohybrid. (c) Low- and (d) high magnification TEM images of $MoS_2/TiO_2$ nanohybrid.

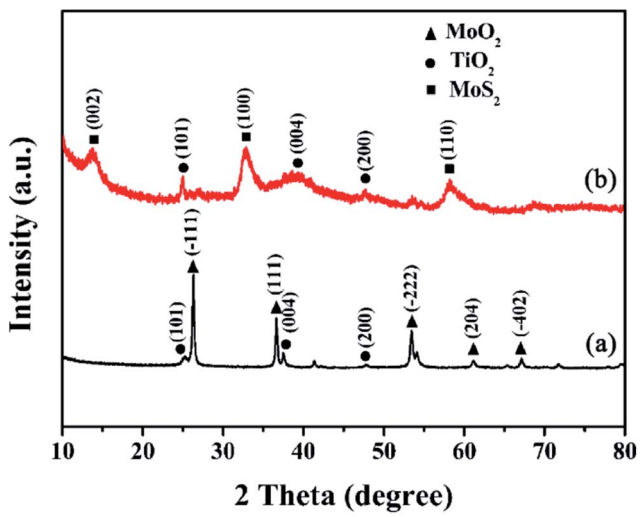


Fig. 2 XRD patterns of (a) precursor of $MoO_2/TiO_2$. (b) As-synthesized $MoS_2/TiO_2$ nanohybrid.

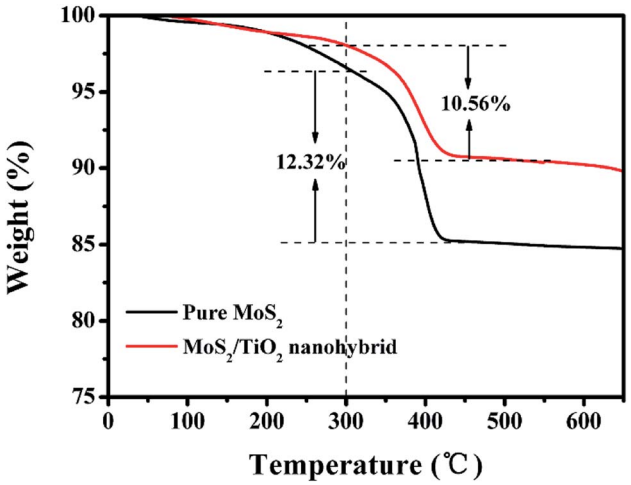


Fig. 4 TGA curves of the $MoS_2/TiO_2$ nanohybrid and pure $MoS_2$ nanoclusters at a temperature ramp of 10 °C $min^{-1}$ in air.

In order to investigate the detailed local elemental composition and distribution of the flower-like $MoS_2/TiO_2$ nanohybrid, energy dispersive X-ray (EDX) mapping analysis was carried out (Fig. 5). The EDS analysis shows that the composite mainly contains O, S, Ti and Mo. Fig. 5b–f shows the full elements map and corresponding elemental mapping images. The O, S, Ti and Mo are homogeneously distributed throughout the samples on the whole. From the elemental mapping, it can be observed that the Mo and S elemental distribution shows strong signals (Fig. 5d and f). For the Ti and O signals, the distinct distributions are sparse compared to Mo and S. It agrees well with the EDS spectrum.

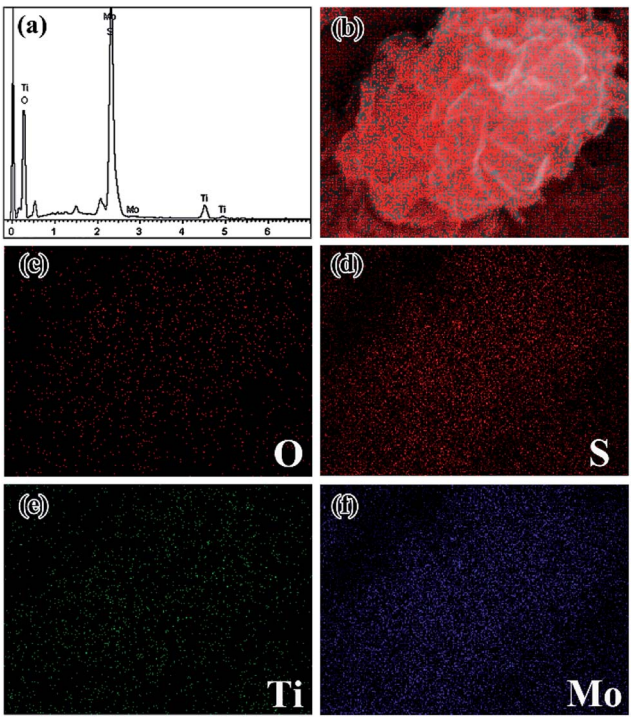


Fig. 5 (a) EDS spectrum of the $MoS_2/TiO_2$ nanohybrid; the EDX elemental maps of (b) full elemental map and the corresponding elemental mapping images of (c) oxygen (d) sulfur (e) titanium and (f) molybdenum.

### 3.2 Electrochemical properties

The annealed $MoS_2/TiO_2$ nanohybrid was assembled into Li half-cells to investigate the electrochemical performance. Fig. 6a shows the cyclic voltammetry curves (CVs) of the annealed $MoS_2/TiO_2$ nanohybrid, which we collected at a scan rate of 0.01 mV $s^{-1}$ in a potential window of 0.01–3.0 V *vs.* $Li^+/Li$. In the first cathodic process (discharge process), four reduction peaks appear at approximately at 1.8 V, 1.7 V, 1.1 V and 0.6 V. The remarkable cathodic peak appears at 1.8 V, indicating the lithiation process leading from S to $Li_2S$.[25] The weak reduction peak at 1.7 V is due to the lithiation of $TiO_2$ nanoparticles. The reduction peak at 1.1 V is attributed to the Li intercalation into the $MoS_2$ nanosheets, resulting in the phase transformation from trigonal prismatic to octahedral.[26] The reduction peak at 0.6 V can be assigned to the decomposition of $Li_xMoS_2$ into $Li_2S$ and Mo particles, which is based on the conversion reaction: $MoS_2 + 4Li^+ + 4e^- \rightarrow Mo + 2Li_2S$.[27] These peaks disappear in the successive cathodic process resulting from few amorphous $MoS_2$ reformed after the first charge process. In the follow cycles, a new reduction peak appears at 1.8 V corresponding to lithiation process of S to form sulfur-containing materials.[25] In the first charge process, three anodic peaks appear at 1.75 V, 2.0 V and 2.3 V. The small oxidation peak at 1.75 V is likely due to the transformation of Mo to $MoS_2$. The two peaks at 2.0 V and 2.3 V are attributed to the reversible conversion reactions of $Li_xTiO_2$ to $TiO_2$ and the conversion of $Li_2S$ into S, respectively. A broad envelope feature at lower potential could be found, which

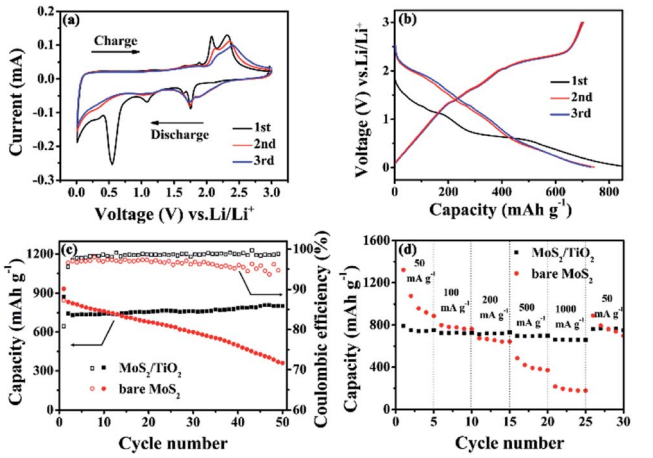


Fig. 6 (a) Representative CV curves for the 1st, 2nd, 3rd of the annealed $MoS_2/TiO_2$ nanohybrid at a scan rate of 0.1 mV $s^{-1}$, (b) galvanostatic charge–discharge voltage profiles of the annealed $MoS_2/TiO_2$ nanohybrid at a current density of 100 mA $g^{-1}$, (c) comparative cycling performance and coulombic efficiency of the annealed $MoS_2/TiO_2$ nanohybrid and bare $MoS_2$ at a current density of 100 mA $g^{-1}$, (d) rate performance of the annealed and bare $MoS_2$ at different current densities.

due to the formation of amorphous phase.[28] The CV curves of bare $MoS_2$ is shown in Fig. S5a.† Compared with $MoS_2/TiO_2$ nanohybrid, the reduction peak at 1.7 V and oxidation peak at 2.0 V are disappeared. It is attributed to the absence of $TiO_2$. Fig. 6b presents the galvanostatic discharge–charge (GDC) voltage profiles of the annealed $MoS_2/TiO_2$ nanohybrid at 100 mA $g^{-1}$. In agreement with the above CV results, two apparent voltage plateaus at 1.1 V and 0.6 V in the first discharge process are attributed to the phase transformation from 2H-$MoS_2$ to 1T-$Li_xMoS_2$ and further conversion into Mo and $Li_2S$. During the charge process, a weak potential plateau at 1.75 V is attributed to the oxidation of Mo to $MoS_2$. The other conspicuous potential plateau at about 2.3 V appeared is corresponding to the conversion of $Li_2S$ into S. There is no obvious difference compared with bare $MoS_2$ (Fig. S5b†). It may be due to relatively low content of $TiO_2$. In the first cycle, the $MoS_2/TiO_2$ nanohybrid reveals discharge and charge specific capacities of 871.4 mA h $g^{-1}$ and 696.7 mA h $g^{-1}$, respectively, leading to a relatively high coulombic efficiency (CE) of 80%. It should be mainly due to the gel-like polymeric layer formation on the $MoS_2/TiO_2$ nanohybrid.[29] The charge and discharge capacities in the second cycle are 743.3 mA h $g^{-1}$ and 702.8 mA h $g^{-1}$, giving a relatively high coulombic efficiency of 94.5%. The cycling performances and coulombic efficiency of $MoS_2/TiO_2$ nanohybrid and bare $MoS_2$ are shown in Fig. 6c. The initial discharge capacity of $MoS_2/TiO_2$ nanohybrid is 871.4 mA h $g^{-1}$, it exhibits lower discharge capacity than the $MoS_2$. This is mainly on account of the influence of the $TiO_2$. Nevertheless, after 50 cycles, the specific capacity of the bare $MoS_2$ decreases quickly from 932.7 mA h $g^{-1}$ to 360.9 mA h $g^{-1}$, while the $MoS_2/TiO_2$ nanohybrid delivers a discharge specific capacity of 802 mA h $g^{-1}$ with a capacity retention of 92%. The $MoS_2/TiO_2$ hybrid nanostructures possess more stable cycle stability and higher discharge capacities than the bare $MoS_2$. The coulombic efficiency of $MoS_2/TiO_2$ hybrid is also higher than bare $MoS_2$. The cycling performance of bare acetylene black and $TiO_2$ were shown in Fig. S6.† We assess that 10 wt% of acetylene black and 14.29 wt% of $TiO_2$ contribute ~40 mA h $g^{-1}$ to the discharge capacity in total. The rate behavior was shown in Fig. 6d. The 3D nanoflower-like $MoS_2/TiO_2$ hybrid displays a reversible discharge capacity of 660 mA h $g^{-1}$ at a current density of 1000 mA $g^{-1}$ and retains a capacity of about 760 mA h $g^{-1}$ as the current density is back to 100 mA $g^{-1}$, indicating the good capacity recovery. Comparably, the bare $MoS_2$ exhibits the inferior cyclic capacity retention and rate capability. The excellent electrochemical performance may be attributed to the favorable synergistic effect between $MoS_2$ and $TiO_2$. The $TiO_2$ nanoparticles can enhance the structure stability and shorten the transport of ions across the surface.

Electrochemical impedance spectroscopy (EIS) was carried out to study the electrode kinetics of the materials (Fig. 7). The Nyquist plots were simulated by the equivalent circuit as depicted in Fig. 7b. $R_e$ represents the resistance contribution from the electrolyte, electrode and the passive film between them. The symbol $R_{sf}$ represented by the semicircle at high frequency are due to the $Li^+$ migration through the solid electrolyte interphase (SEI) film. The symbol $R_{ct}$ are assigned to the charge-transfer

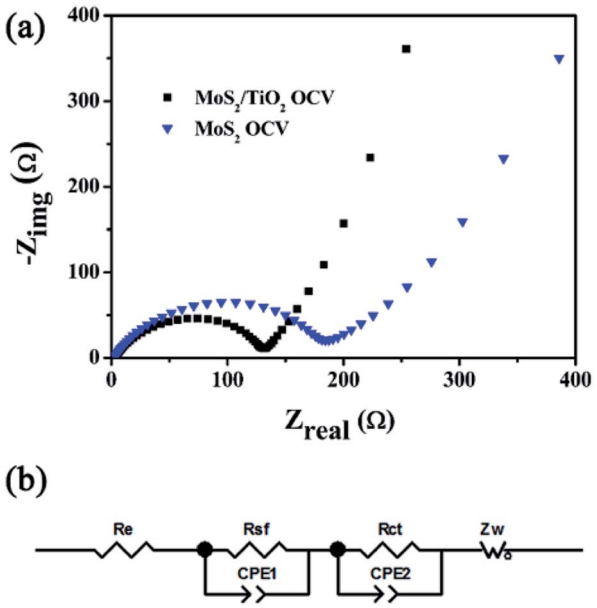


Fig. 7 (a) Nyquist plots of the $MoS_2/TiO_2$ hybrid and bare $MoS_2$ electrodes, (b) equivalent circuits for fitting Nyquist plots.

resistance at the electrode/electrolyte interface, which is shown by a semicircle in mid-frequency region. The slope line in the low frequency region relates to $Li^+$ diffusion processes in the active material. The EIS experiments of $MoS_2/TiO_2$ hybrid and bare $MoS_2$ were conducted at OCV (open circuit potential) firstly (Fig. 7a). As can be seen, the $MoS_2/TiO_2$ hybrid shows a smaller semicircle diameter than the $MoS_2$, indicating that the $MoS_2/TiO_2$ hybrid has lower charge transfer resistance. The charge-transfer resistance ($R_{ct}$) of the $MoS_2/TiO_2$ hybrid and $MoS_2$ are 120.9 Ω and 148.8 Ω, respectively. Fig. S7† shows the Nyquist plot for the $MoS_2/TiO_2$ hybrid and bare $MoS_2$ after the first discharge and charge process. The impedance data values are summarized in Table S1.† At the end of the 1st discharge, the semicircle at high frequency appears because of the resistance of surface-passivation layer.[30] The $R_{sf}$ of $MoS_2/TiO_2$ hybrid and $MoS_2$ are 37.6 Ω and 108.2 Ω, respectively. Such phenomenon indicates the formation of a thick SEI layer on the surface.[31] Therefore, the decreasing tendency of $R_{ct}$ could be observed. However, the $R_{ct}$ of $MoS_2/TiO_2$ hybrid (114.9 Ω) is also much lower than $MoS_2$ (138.5 Ω). After the 1st charge, the diameter of semicircle at mid-frequency is significantly enlarged. The increasing charge transfer resistance may due to the volume expansion of $MoS_2$ after the first cycle. Nevertheless, the $MoS_2/TiO_2$ (195.4 Ω) shows a smaller semicircle diameter than the $MoS_2$ electrode (259.7 Ω), indicating that the $MoS_2/TiO_2$ hybrid has lower charge transfer resistance ($R_{ct}$). The effect of the modification with $TiO_2$ may be verified. The modification of $TiO_2$ may stabilize the structure of $MoS_2$ and alleviate volume change. The $MoS_2/TiO_2$ hybrid shows lower slope than bare $MoS_2$, indicating the better lithium ion kinetics in the electrode materials. It may due to attachment of $TiO_2$ particles onto the surface of $MoS_2$ can greatly enhance electron transport. Consequently, a favorable synergistic effect between the $TiO_2$ nanoparticles and $MoS_2$ nanosheets is supposed.

## 4. Conclusions

In summary, $TiO_2$ nanoparticles decorated $MoS_2$ nanoflowers have been successfully developed by a two-step hydrothermal process. As the anode materials for LIBs, the electrochemical performance of $MoS_2/TiO_2$ hybrid is better than bare $MoS_2$. This may be due to the hybridization with $TiO_2$ be able to stabilize the structure of $MoS_2$ and effectively accommodates the volume changes. Meanwhile, the $TiO_2$ nanoparticles can shorten the transport of ions across the surface. This work opens up an avenue for the rational design of other anode composite materials in high performance LIBs.

## Acknowledgements

We appreciate the financial support of the NSFC (U1503391).

## Notes and references

1 X. Cao, Y. Shi, W. Shi, X. Rui, Q. Yan, J. Kong and H. Zhang, *Small*, 2013, **9**, 3433–3438.
2 Y. Xu, G. Yin, Y. Ma, P. Zuo and X. Cheng, *J. Mater. Chem.*, 2010, **20**, 3216–3220.
3 T. Stephenson, Z. Li, B. Olsen and D. Mitlin, *Energy Environ. Sci.*, 2014, **7**, 209–231.
4 X. Xu, W. Liu, Y. Kim and J. Cho, *Nano Today*, 2014, **9**, 604–630.
5 J. Ye, L. Ma, W. Chen, Y. Ma, F. Huang, C. Gao and J. Y. Lee, *J. Mater. Chem. A*, 2015, **3**, 6884–6893.
6 H. Hwang, H. Kim and J. Cho, *Nano Lett.*, 2011, **11**, 4826–4830.
7 X. Li, W. Li, M. Li, P. Cui, D. Chen, T. Gengenbach, L. Chu, H. Liu and G. Song, *J. Mater. Chem. A*, 2015, **3**, 2762–2769.
8 S.-K. Park, S.-H. Yu, S. Woo, J. Ha, J. Shin, Y.-E. Sung and Y. Piao, *CrystEngComm*, 2012, **14**, 8323–8325.
9 U. K. Sen and S. Mitra, *ACS Appl. Mater. Interfaces*, 2013, **5**, 1240–1247.
10 S. Wang, X. Jiang, H. Zheng, H. Wu, S.-J. Kim and C. Feng, *Nanosci. Nanotechnol. Lett.*, 2012, **4**, 378–383.
11 Z. Hu, L. Wang, K. Zhang, J. Wang, F. Cheng, Z. Tao and J. Chen, *Angew. Chem.*, 2014, **126**, 13008–13012.
12 G. Tang, J. Sun, C. Wei, K. Wu, X. Ji, S. Liu, H. Tang and C. Li, *Mater. Lett.*, 2012, **86**, 9–12.
13 S. Ding, J. S. Chen and X. W. D. Lou, *Chem.–Eur. J.*, 2011, **17**, 13142–13145.
14 L. Zhang, W. Fan, W. W. Tjiu and T. Liu, *RSC Adv.*, 2015, **5**, 34777–34787.
15 G.-H. Lee, S.-J. Kim, M.-C. Kim, H.-S. Choe, D.-M. Kim, S.-B. Han, D.-H. Kwak, J. H. Jeong and K.-W. Park, *RSC Adv.*, 2016, **6**, 92259–92266.
16 L. Hu, Y. Ren, H. Yang and Q. Xu, *ACS Appl. Mater. Interfaces*, 2014, **6**, 14644–14652.
17 L. Yang, S. Wang, J. Mao, J. Deng, Q. Gao, Y. Tang and O. G. Schmidt, *Adv. Mater.*, 2013, **25**, 1180–1184.
18 Y. Chen, B. Song, X. Tang, L. Lu and J. Xue, *Small*, 2014, **10**, 1536–1543.
19 B. Chen, N. Zhao, L. Guo, F. He, C. Shi, C. He, J. Li and E. Liu, *Nanoscale*, 2015, **7**, 12895–12905.
20 X. Xu, Z. Fan, S. Ding, D. Yu and Y. Du, *Nanoscale*, 2014, **6**, 5245–5250.
21 Q. Xiang, J. Yu and M. Jaroniec, *J. Am. Chem. Soc.*, 2012, **134**, 6575–6578.
22 Q. Pang, Y. Zhao, X. Bian, Y. Ju, X. Wang, Y. Wei, B. Liu, F. Du, C. Wang and G. Chen, *J. Mater. Chem. A*, 2017, **5**, 3667–3674.
23 X. Zhu, C. Yang, F. Xiao, J. Wang and X. Su, *New J. Chem.*, 2015, **39**, 683–688.
24 C. Liu, L. Wang, Y. Tang, S. Luo, Y. Liu, S. Zhang, Y. Zeng and Y. Xu, *Appl. Catal., B*, 2015, **164**, 1–9.
25 W. Zhuang, L. Li, J. Zhu, R. An, L. Lu, X. Lu, X. Wu and H. Ying, *ChemElectroChem*, 2015, **2**, 374–381.
26 G. Du, Z. Guo, S. Wang, R. Zeng, Z. Chen and H. Liu, *Chem. Commun.*, 2010, **46**, 1106–1108.
27 M. Mao, L. Mei, D. Guo, L. Wu, D. Zhang, Q. Li and T. Wang, *Nanoscale*, 2014, **6**, 12350–12353.
28 T.-F. Yi, J.-Z. Wu, M. Li, Y.-R. Zhu, Y. Xie and R.-S. Zhu, *RSC Adv.*, 2015, **5**, 37367–37376.
29 K. Chang and W. Chen, *ACS Nano*, 2011, **5**, 4720–4728.
30 B. Chen, N. Zhao, L. Guo, F. He, C. Shi, C. He, J. Li and E. Liu, *Nanoscale*, 2015, **7**, 12895–12905.
31 T. S. Sahu and S. Mitra, *Sci. Rep.*, 2015, **5**, 12571.

 